Lehrstuhl für Bildverarbeitung
Institute of Imaging & Computer Vision

Digital Image Acquisition and Processing in Medical X-Ray Imaging

Til Aach and Ulrich Schiebel and Gerhard Spekowius

in: Journal of Electronic Imaging. See also BIBTEX entry below.

BIBTEX:

```
@article{AAC99a,
author = {Til Aach and Ulrich Schiebel and Gerhard Spekowius},
title = {Digital Image Acquisition and Processing in Medical
   X-Ray Imaging},
journal = {Journal of Electronic Imaging},
        publisher       = {SPIE},
volume = {8},
number = {Special Section on Biomedical Image Representation},
year = {1999},
pages = {7--22}}
```


document created on: December 20, 2006
created from file: jei97coverpage.tex
cover page automatically created with CoverPage.sty
(available at your favourite CTAN mirror)

RWTH AACHEN
RHEINISCH-WESTFÄLISCHE TECHNISCHE HOCHSCHULE AACHEN

A reprint from

JOURNAL OF

Electronic Imaging

ISSN 1017-9909

January 1999

Digital image acquisition and processing in medical x-ray imaging

Til Aach
Ulrich Schiebel
Gerhard Spekowius

Journal of Electronic Imaging 8(1), 7–22 (January 1999).

Digital image acquisition and processing in medical x-ray imaging*

Til Aach†
Ulrich Schiebel
Gerhard Spekowius
Philips GmbH Research Laboratories
Weisshausstrasse 2
D-52066 Aachen, Germany
E-mail: aach@informatik.mu-luebeck.de

Abstract. *This contribution discusses a selection of today's techniques and future concepts for digital x-ray imaging in medicine. Advantages of digital imaging over conventional analog methods include the possibility to archive and transmit images in digital information systems as well as to digitally process pictures before display, for example, to enhance low contrast details. After reviewing two digital x-ray radiography systems for the capture of still x-ray images, we examine the real time acquisition of dynamic x-ray images (x-ray fluoroscopy). Here, particular attention is paid to the implications of introducing charge-coupled device cameras. We then present a new unified radiography/fluoroscopy solid-state detector concept. As digital image quality is predominantly determined by the relation of signal and noise, aspects of signal transfer, noise, and noise-related quality measures like detective quantum efficiency feature prominently in our discussions. Finally, we describe a digital image processing algorithm for the reduction of noise in images acquired with low x-ray dose.* © 1999 SPIE and IS&T.
[S1017-9909(99)00401-8]

1 Introduction and Overview

In this paper, we discuss selected current topics of digital image acquisition and processing in medicine, focusing on x-ray projection imaging. A key feature of digital imaging is the inherent separation of image acquisition and display. Whereas analog screen/film combinations (Fig. 1) use film as a medium for both image recording and viewing, digitally acquired images can be processed in order to correct accidental over- or underexposure, or to enhance diagnostically relevant information before display. Also, digital images can be stored and transmitted via picture archiving and communication systems (PACS),[1] and be presented on different output devices, like film printers or cathode ray tube (CRT) monitors (*softcopy viewing*).

The separation of image acquisition and display in a digital system is illustrated by comparing analog and digital acquisition of single high resolution projection images (*x-ray radiography*). The principle of the imaging setup is sketched in Fig. 2. X radiation passes through the patient before exposing a detector. Widely used for image detection are analog screen/film combinations as shown in Fig. 1, which consist of a film sheet sandwiched between thin phosphor intensifying screens. The phosphor screens convert the incoming x radiation into visible light blackening the film, which, after developing, is examined by viewing on a lightbox.

Well-established digital alternatives include storage phosphor systems (SPS),[2–4] also known as computed radiography (CR) systems, and a selenium-detector based digital chest radiography system [(DCS), "Thoravision"].[5,6] In CR systems, the image receptor is a photostimulable phosphor plate, which absorbs and stores a significant portion of the incoming x-ray energy by trapping electrons and holes in elevated energy states. The stored energy pattern can be read out by scanning the plate with a laser beam. The emitted luminescence is detected by a photomultiplier and subsequently digitized. Common plate sizes are 35×35 cm^2 sampled by a 1760×1760 matrix, 24×30 cm^2 sampled by a 1576×1976 matrix, and for high resolutions 18×24 cm^2 sampled by a 1770×2370 matrix. The resulting Nyquist frequencies are between 2.5 and 5 lp/mm. An example CR image is given in Fig. 3.

The detector of a DCS consists of an amorphous selenium layer evaporated onto a cylindrical aluminum drum. Exposure of the drum to x radiation generates an electrostatic charge image, which is read out by electrometer sensors. Maximum size of the sampled image matrix is 2166×2448 pixels, with a Nyquist frequency of 2.7 lp/mm.

In analog as well as in digital systems, the acquired radiographs are degraded by nonideal system properties. These include limitations of contrast and resolution, and are described for instance by the modulation transfer function (MTF). Other undesired effects are spatially varying detector sensitivity and unwanted offsets. Additional degradations can be introduced by accidental over- or underexpo-

*Partly presented as an invited paper at the International Symposium on Electronic Photography (ISEP: a PHOTOKINA event), Cologne, Germany, Sept. 21–22, 1996.

†T. Aach is now with the Medical University of Luebeck, Institute for Signal Processing and Process Control, Ratzeburger Allee 160, D-23538 Luebeck, Germany.

Paper 97010 received Apr. 1, 1997; revised manuscript received May 1, 1998; accepted for publication June 1, 1998.
1017-9909/99/$10.00 © 1999 SPIE and IS&T.

Fig. 1 Principle of conventional x-ray image detection by a screen/film combination. The light-sensitive film is sandwiched between two phosphor intensifying screens which convert the incoming x radiation into visible light.

sure. Unlike screen/film systems, however, digital systems enable the compensation of such known degradations by suitable processing like gain and offset correction and MTF restoration. Furthermore, the problem of over- or underexposures is virtually eliminated by the wide latitude of the SPS and DCS image receptors (about four orders of magnitude) and the possibility to digitally adjust the displayed intensity range. Finally, methods like "unsharp masking" and "harmonization" can be employed to enhance relevant detail with respect to diagnostically less important information, and to optimize image presentation on the selected output device.[7–10] Figure 4 shows the result of applying such enhancement techniques to the radiograph in Fig. 3.

As we will see, the predominant factor limiting the extent up to which MTF restoration and optimization of image presentation can be successful is the noise level present in a digital image. Rather than by traditional quality measures like MTF or radiographic speed of screen/film combinations, the imaging performance of electronic systems is therefore described by measures capturing the signal-to-noise transfer properties, like signal-to-noise ratio (SNR), noise equivalent quanta (NEQ) and detective quantum efficiency (DQE).[3,6,11] An imaging-inherent noise source is the discrete nature of x radiation, generating so-called x-ray *quantum noise* in the acquired images. This type of noise is particularly relevant for images recorded with very low x-radiation doses, and affects both analog and digital imaging systems. Clearly, noise introduced within the imaging system during later processing stages, e.g., quantization noise during analog-to-digital (A/D) conversion, can further deteriorate the imaging performance. Noise behavior therefore features prominently in our discussions.

In the next section we review x-ray image quality measures needed later in the paper. We then consider digital real time dynamic x-ray imaging, known as x-ray *fluoroscopy*. Here, we pay particular attention to differences in noise behavior of electronic camera tubes (Sec. 3.3) and solid-state charge-coupled device (CCD) cameras (Sec. 3.4). This is followed by a discussion of a new flat solid-state x-ray sensor for both digital x-ray fluoroscopy and high resolution radiography. Finally, in Sec. 5, we describe a recently developed quantum noise reduction filter.

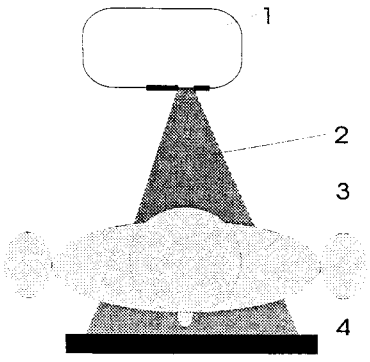

Fig. 2 Principle of x-ray projection radiography (view from above, 1: x-ray tube, 2: x-ray beam, 3: patient, 4: detector).

Fig. 3 Portion of size 700×1846 pixels from a radiograph of a foot (dorso-plantar) acquired by a CR system.

2 X-Ray Image Detection

An x-ray tube generates x radiation by accelerating electrons in an electric field towards a tungsten anode. On hitting the anode, about 1% of the electrons generate x-ray quanta, which leave the tube through an x-ray transparent window. The x-ray beam consists of a discrete number of x-ray quanta of varying energy, with the maximum energy being limited by the applied tube voltage. Typical values for the tube voltage range between 60 and 150 kV. The energy distribution of the x-ray quanta determines the *beam quality*. A thin aluminum plate about 3 mm thick, which absorbs low-energy x-ray quanta unable to pass through the patient, is integrated directly into the tube window. These

Fig. 4 Enhanced version of Fig. 3. First, middle and high spatial frequencies were amplified relative to very low ones in order to make such details better visible (*harmonization*). In a second stage, the image was given a sharper appearance by additional amplification of high spatial frequencies by *unsharp masking*.

quanta would only add to the absorbed patient dose without contributing to the imaging process. In the following, the thus reduced range of energies is approximated by a single, average energy, i.e., we assume monoenergetic x radiation. For tube voltages of 150 and 60 kV, these average energies are about 63 and 38 keV, respectively.

Owing to the discrete nature of x radiation only a limited, potentially small number of x-ray quanta contributes to the imaging process at each pixel. For instance, in x-ray fluoroscopy the typical x-ray dose for an image is about 10 nGy at a beam quality of 60 keV. This results in a quantum flow q_0 of roughly $q_0 = 300$ quanta/mm^2. X-ray quantum noise is caused by random fluctuations of the quantum flow, which obey a Poisson distribution.[12] Therefore, the standard deviation σ of quantum noise is proportional to $\sqrt{q_0}$. As the detected signal S is proportional to q_0, the

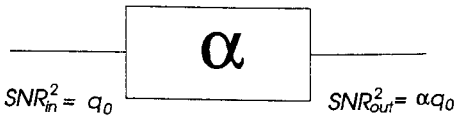

Fig. 5 Schematic diagram of an efficiency stage of an x-ray detector, which absorbs only a fraction α of the incoming quantum flow q_0.

SNR S/σ varies with $\sqrt{q_0}$, and decreases with decreasing x-ray dose.

A real detector absorbs only a fraction of the incoming x-ray quanta given by the detector *absorption efficiency* α (Fig. 5). The squared signal-to-noise ratio at the output of this *efficiency stage* obeys

$$\mathrm{SNR}_{out}^2 = \frac{S_{out}^2}{\sigma_{out}^2} = \frac{\alpha^2 q_0^2}{\alpha q_0} = \alpha q_0, \tag{1}$$

and is equal to the effective number of absorbed x-ray quanta. The squared SNR is therefore also referred to as *noise equivalent quanta* (NEQ). Normalizing SNR_{out}^2 by q_0 yields the so-called *detective quantum efficiency* (DQE). For the efficiency stage in Fig. 5, the DQE is identical to the absorption efficiency α. As q_0 corresponds to the squared input SNR, the DQE can also be interpreted as the ratio $\mathrm{SNR}_{out}^2/\mathrm{SNR}_{in}^2$.

The so far simplified treatment of NEQ and DQE considered only homogeneous exposures with a spatially constant quantum flow q_0, and neglected noise generated by the detector system. In the following, we present more general definitions of spatial frequency-dependent NEQ and DQE for electronic imaging systems, including effects of a nonideal detector MTF and detector noise. The original definitions of NEQ and DQE for *photographic* systems can be found in Refs. 13 and 14 (cf. also Ref. 11).

Figure 6 shows the diagram of our detector model. The efficiency stage is followed by a gain factor G, which describes the conversion of x-ray quanta into other information carriers, e.g., electrons for the solid-state detector discussed in Sec. 4. This is followed by a stage of spatially scattering the information carriers, which results in a spatial blur. This is described by a linear modulation transfer function (MTF) $H(u)$, which decreases over the spatial frequency u. Finally, system noise with power spectrum $N_{sys}^2(u)$ is added. The power spectrum N_q^2 of the incoming quantum noise is flat,[15] and its power spectral density is shown in Appendix A to be equal to the quantum flow q_0.

Clearly, at zero spatial frequency, i.e., for a homogeneous exposure with quantum flow q_0, the output signal is given by

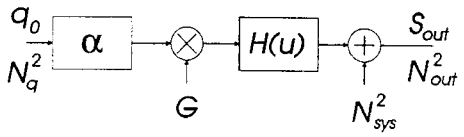

Fig. 6 Schematic of an x-ray detector comprising an efficiency stage followed by a conversion with gain G, a linear MTF $H(u)$, and additive system noise with NPS N_{sys}^2.

$$S_{out}(0) = q_0 \alpha G, \tag{2}$$

since $H(0) = 1$. Noise at the detector output consists of the originally white quantum noise filtered by the system transfer function and of system noise. Its power spectrum $N^2_{out}(u)$ is

$$N^2_{out}(u) = q_0 \alpha G^2 H^2(u) + N^2_{sys}(u). \tag{3}$$

We now consider an almost homogeneous exposure with a sinusoidally varying quantum flow $q(u,x) = q_0[1 + \epsilon \sin(2\pi u x)]$, where x is a spatial coordinate, and $0 < \epsilon \ll 1$. This exposure is recorded with the same x-ray dose as the previous homogeneous exposure, since the spatially averaged quantum count $\bar{q}(u)$ is identical to q_0. The output amplitude $S_{out}(u)$ of the sinusoid component is given by

$$S_{out}(u) = q_0 \epsilon \alpha G H(u). \tag{4}$$

The noise equivalent quanta $\mathrm{NEQ}_{out}(u)$ as a function of spatial frequency is now defined as

$$\mathrm{NEQ}_{out}(u) = q_0 \frac{\mathrm{SNR}^2_{out}(u)}{\mathrm{SNR}^2_{in}(u)} = \frac{q_0^2 \alpha^2 G^2 H^2(u)}{q_0 \alpha G^2 H^2(u) + N^2_{sys}(u)}. \tag{5}$$

To interpret this quantity, we consider the case of vanishing system noise, that is, $N^2_{sys}(u) = 0$ for all u. Both signal and noise are then filtered by the same transfer function $H(u)$, resulting in $\mathrm{NEQ}_{out}(u) = \alpha q_0$, which does not depend on u anymore. Assuming that the MTF $H(u)$ is different from zero for all u, the original signal can be restored by inverse filtering with $H^{-1}(u)$. Simultaneously, this operation transforms the lowpass-shaped noise power spectrum (NPS) $N^2_{out}(u)$ again into a flat NPS.

Nonvanishing system noise decreases the NEQ, especially at those spatial frequencies where $N^2_{sys}(u)$ exceeds the filtered quantum noise spectrum. As in practice system noise is often white, this is generally the case for higher spatial frequencies, where the filtered quantum noise spectrum is small. Restoration by inverse filtering would now result in unacceptably boosted system noise.

As before, the detective quantum efficiency is defined as noise equivalent quanta normalized by the spatially averaged incoming quantum flow q_0:

$$\mathrm{DQE}(u) = \frac{\mathrm{NEQ}_{out}(u)}{q_0} = \frac{\mathrm{SNR}^2_{out}(u)}{\mathrm{SNR}^2_{in}(u)} = \frac{q_0 \alpha^2 G^2 H^2(u)}{q_0 \alpha G^2 H^2(u) + N^2_{sys}(u)}. \tag{6}$$

Example DQE curves for a real system are given below (Fig. 16). Denoting the output NPS in the ideal case of vanishing system noise by $N^2_{id}(u)$, the DQE can be rewritten as

$$\mathrm{DQE}(u) = \alpha \frac{N^2_{id}(u)}{N^2_{out}(u)}. \tag{7}$$

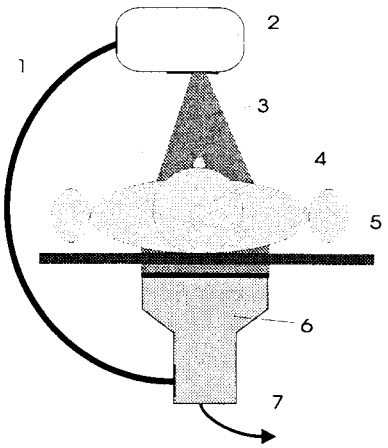

Fig. 7 Sketch of a fluoroscopy system [1: movable C arm, 2: x-ray tube, 3: x-ray beam, 4: patient, 5: operating table, 6: detection front end, 7: video signal fed to processing unit and monitor (not shown)].

Hence, the larger the actually encountered output noise in relation to the filtered quantum noise, the lower the DQE is.

From Eq. (7), a measure can be derived which indicates how far linear signal restoration is possible without disproportionate noise amplification. Requiring the NPS after restoration to be flat, the following restoration filter $H_R(u)$ can easily be derived:

$$H_R(u) = \sqrt{\frac{\mathrm{DQE}(u)}{\mathrm{DQE}(0)}}\, H^{-1}(u). \tag{8}$$

Evidently, low values for DQE(u)—caused by increased noise levels—allow only a correspondingly lower restoration to be applied. For a noiseless ideal system, the DQE in Eq. (8) is frequency independent and permits full restoration by inverse filtering.

3 Digital X-Ray Fluoroscopy

X-ray fluoroscopy is a real time dynamic x-ray imaging modality which allows a physician to monitor on-line clinical procedures like catheterization or injection of contrast agents. An x-ray fluoroscopy system is sketched in Fig. 7: a movable C-shaped arm bearing the x-ray tube and the image detection "front end" is mounted close to the operating table. The position of the C arm can be adjusted arbitrarily during the clinical procedure. The detected dynamic images are displayed on a CRT monitor placed near the operating table, hence providing the physician with immediate visual feedback.

3.1 *Fluoroscopy Image Detection*

Today's detection front ends consist of an x-ray image intensifier (XRII) coupled by a tandem lens to a TV camera,[16,17] which is followed by an A/D converter (Fig. 8). The XRII is a vacuum tube containing an entrance screen attached directly to a photocathode, an electron optics, and a phosphor screen output window. Images are detected by a fluorescent caesium iodide (CsI) layer on the entrance screen, which converts the incoming x-ray quanta

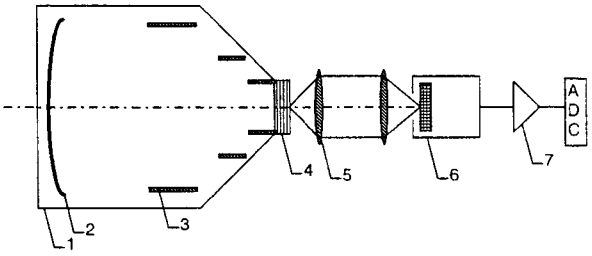

Fig. 8 Detector front end of a fluoroscopy system (1: XRII tube, 2: input screen and photocathode, 3: electron optics, 4: output window, 5: tandem lens, 6: TV camera, 7: amplifier).

into visible photons, which in turn reach the photocathode. The CsI screen is a layer approximately 400 μm thick and evaporated onto an aluminum substrate. The absorption of these screens is about 60%–70%.[16,18] In addition, as shown in Fig. 9, CsI is grown in a needle-like structure such that the individual needles act as optical guides for the generated light photons. This prevents undesired lateral propagation within the CsI layer, and thus ensures a relatively good screen MTF (see Fig. 13).

The generated photoelectrons are accelerated when passing through the electron optics and focused onto the output window, where they generate luminescence photons. The resulting visible pictures are then picked up by the camera. The diameter of the circular XRII entrance screen ranges between 15 and 40 cm, depending on the application, while the diameter of the XRII output window is between 25 and 50 mm. Apart from image intensification, the electron optics allow demagnification, and zooming by projecting a small subfield of the entrance screen onto the output window.

To pick up the images from the XRII output window, electronic camera tubes like plumbicons, vidicons or saticons are still in wide use today. In Europe, camera readout is mostly with 625 lines/image, with the full frame rate of 25 images per second in interlaced or progressive format. However, special high resolution modes (1250 lines/image) are also often available. In applications where temporal resolution is less critical, the frame rate can be reduced down to only a single image per second (*low frame rate pulsed fluoroscopy*) in order to save x-ray dose. The analog

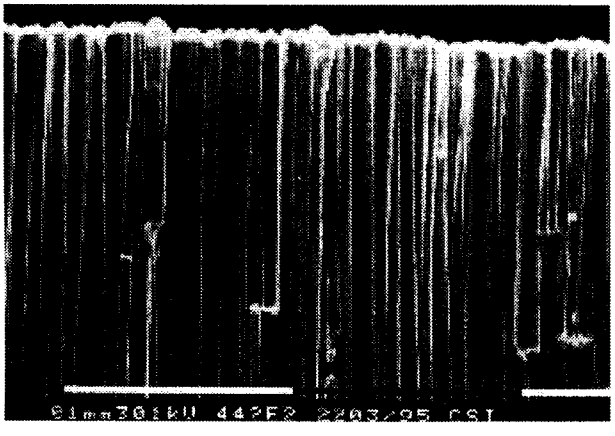

Fig. 9 Electron-microscopic image of the cross section of a CsI layer.

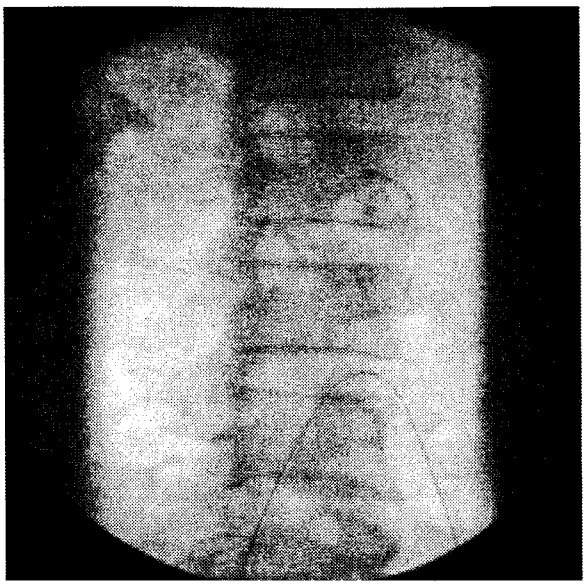

Fig. 10 Sample image from a fluoroscopy sequence, partly showing a patient's spine and a guidewire. The circular image boundary is caused by the cylindrical shape of the XRII.

video signal is then amplified and fed to an 8 bit–10 bit A/D converter. In case of digitization by 8 bit, the gain of the amplifier is higher for smaller signal amplitudes than for larger ones in order to enhance dark parts of the images. This is commonly referred to as *analog white compression*. An example of a fluoroscopy image is depicted in Fig. 10.

3.2 *Main Noise Sources in Fluoroscopy Image Detection*

The SNR attainable in fluoroscopy is inherently limited by the low x-ray quantum flow q_0, which, as discussed in Sec. 2, generates relatively strong quantum noise in relation to signal.

System-internal noise sources include so-called *fixed pattern noise*, and signal shot noise. Fixed pattern noise is mainly caused by inhomogeneities of the XRII output screen, which are stable over time. Signal shot noise is generated by the discrete nature of the conversion of information carriers, e.g., from luminescence photons into electrons in the XRII photocathode and the camera. As the power spectrum of signal shot noise is approximately flat, while the spectrum of quantum noise is lowpass shaped, shot noise can affect the SNR and the DQE mostly for high spatial frequencies. Still, signal shot noise is often negligible compared to x-ray quantum noise.

3.3 *Noise in Camera Tubes*

The visible images are projected from the XRII output window onto the photoconductive target layer of the camera tube, which for plumbicons, consists of lead oxide (PbO). The resulting electrostatic charge image is then read out by scanning the target layer linewise with an electron beam (*scanned device*). Line-by-line scanning means that sampling in the vertical direction is carried out directly on the photoconductive target, with the size of the electron beam spot being sufficiently large to prevent alias. Horizontal sampling is done later at the A/D converter.

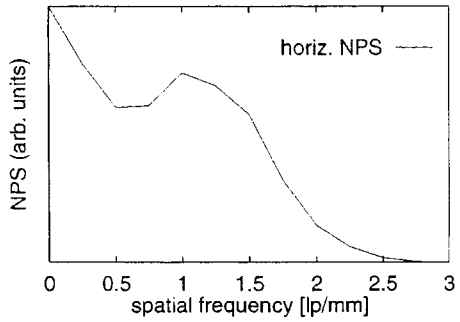

Fig. 11 Horizontal cross section of an NPS for an XRII/camera tube system *before* horizontal sampling. The rise of the NPS between 0.5 and 1.0 lp/mm is due to the highpass characteristic of the amplifier, which compensates the lowpass transfer function of the plumbicon target layer. The NPS drops off again for frequencies larger than 1 lp/mm due to bandwidth limitations and the antialias filter.

Unavoidable capacitances of the target layer itself as well as of the subsequent first amplifier stage act as a lowpass filter, which attenuates high frequency signal components. This attenuation has to be compensated by a highpass-like transfer function of the amplifier, which, however, also amplifies high-frequency components of originally white electronic noise. This effect is referred to as *triangular noise*,[19] because bandwidth limitations and an antialias filter before the A/D converter decrease the noise amplification again for higher spatial frequencies. The overall effect is a triangle-shaped NPS as illustrated in Fig. 11, giving this type of noise its name. Due to the linewise scanning, triangular noise increases only with horizontal spatial frequencies, and is independent of vertical spatial frequencies in the two-dimensional spectral domain.

A typical overall Fourier amplitude spectrum of a homogeneous x-ray exposure acquired by an XRII/plumbicon chain is shown in Fig. 12, where the gray level represents the modulus of the Fourier coefficients. The origin (0,0) of the spatial frequency axes u,v is in the center of the plot. To avoid an excessive peak at the origin, the average image intensity was subtracted prior to the Fourier transform. Hence, the shown amplitude spectrum corresponds to the observed realization of noise in the homogeneous exposure. First, a concentration of high Fourier amplitudes can be observed around the origin, i.e., for low spatial frequencies. This is caused by x-ray quantum noise, and reflects the drop of the overall system MTF toward higher spatial frequencies. Along the horizontal direction, spectral amplitudes increase again toward higher spatial frequencies, reflecting triangular noise. As discussed in the previous paragraph, triangular noise does not occur along the vertical spatial frequency axis.

3.4 *Noise in CCD-Cameras*

Although today's XRII/camera tube combinations achieve a good fluoroscopic image quality, it is intended to introduce high resolution solid-state CCD sensors into future systems in order to further improve image quality. A CCD consists of a two-dimensional (2D) array of discrete sensor elements rather than of a "continuous" target plate. The array size is usually 512×512 or 1 k×1 k sensor elements, each of which corresponds to a pixel. The benefits of using

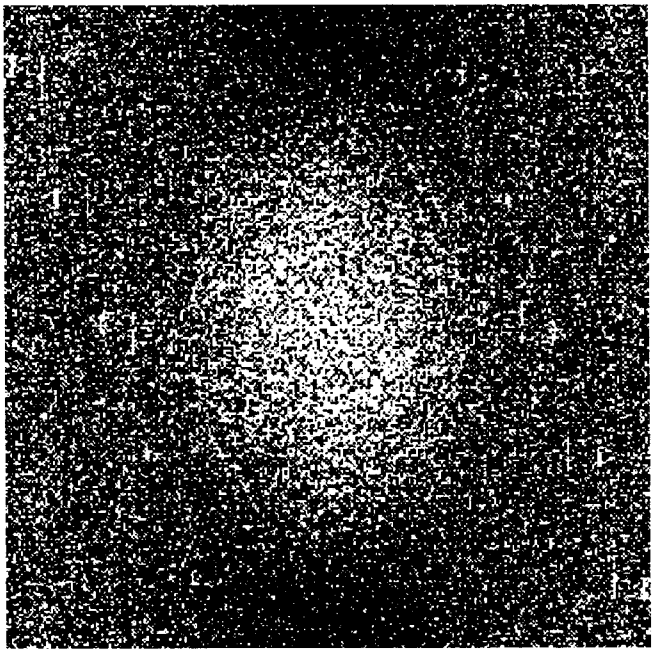

Fig. 12 Two-dimensional Fourier amplitude spectrum of a homogeneous exposure recorded with an XRII/plumbicon chain. The origin of the spatial frequency axes is in the center of the plot. The lowpass-shaped quantum noise spectrum, and, in horizontal direction, triangular noise are plainly evident.

a CCD include greater geometrical stability and the absence of readout jitter. (In an electronic camera tube, readout jitter is caused by instability of the electron readout beam.) First, this improves the performance of subtraction fluoroscopy modalities, like digital subtraction angiography, where a background image is subtracted from live images to increase detail contrast. Second, the increased geometrical stability facilitates the correction of XRII fixed pattern noise. Note that inhomogeneities of the CCD sensor elements may also require a fixed pattern noise correction. Additionally, CCD cameras exhibit less temporal lag than pickup tubes. [Among the mentioned pickup tubes (plumbicons, vidicons, saticons), plumbicons have lowest lag.] This results in less blurring of moving objects, but increased noise levels due to the reduced temporal integration.[20]

The fact that spatial sampling is inherent in a CCD camera causes its noise behavior to be fundamentally different from that of pickup tubes. The Nyquist frequency u_N corresponding to the sampling raster is commonly related to the XRII entrance plane, and depends on the resolution (512×512 or 1 k×1 k pixels), and the selected XRII zoom. It ranges between 0.7 and 4 lp/mm. Apart from the XRII and tandem lens, the presampling system MTF is determined by the aperture of each sensor element, which, for an ideal sensor, is sinc shaped (Fig. 13). However, as can be seen from the MTF for a CCD-pixel aperture in Fig. 13, integration over the sensor element aperture is generally not sufficient to reduce the MTF for spatial frequencies beyond the Nyquist frequency to prevent alias. Hence, if the system MTF is not low (about 5% or less) at u_N, noise (and signal) from beyond u_N is mirrored back to lower spatial frequencies, where it increases the observed noise contributions.

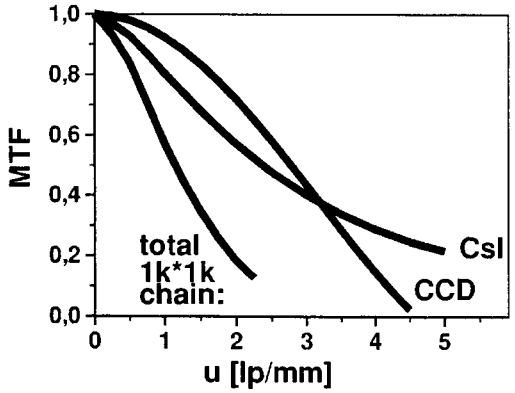

Fig. 13 Sinc-shaped MTF of the finite aperture of a CCD pixel. Also shown are the MTFs of the CsI screen and of the total imaging chain for a Nyquist frequency of 2.2 lp/mm. At this frequency, the pixel MTF is still quite high.

This effect is depicted in Fig. 14. In a pickup tube, such aliasing is prevented by the size of the electron beam spot and by the antialias filter before sampling the video signal. Triangular noise does not occur in a CCD camera.

A particular alias-based distortion can occur when an antiscatter grid is used in connection with a CCD camera.[21] An antiscatter grid consists of thin lead stripes separated by x-ray transparent spacing material, and is mounted close to the XRII entrance screen to prevent x-ray quanta scattered by the patient from reaching the CsI layer. In small XRII modes, i.e., when zooming to a small subfield of the entrance screen, the CCD-pixel size—as related to the entrance plane—approaches the antiscatter grid spacing. As a result, Moiré patterns may occur.

Further CCD-camera noise sources include electron dark current and electronic amplifier noise. The power spectrum of these noise sources is approximately flat up to the Nyquist frequency.

Similar as in Fig. 12 for pickup tubes, Fig. 15 shows the Fourier amplitude spectrum of a homogeneous exposure recorded by an XRII/CCD chain. The influence of the low-pass shaped quantum noise spectrum is clearly evident, as is the absence of triangular noise. Quantum noise extends to higher spatial frequencies than in Fig. 12, this is mostly due to the significantly better MTF of a CCD as compared to a pickup tube.

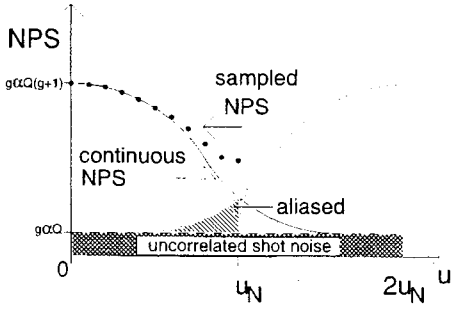

Fig. 14 NPS aliasing effects induced by sampling in a CCD. This figure depicts the continuous NPS and its shifted version located at the sampling frequency $2u_N$. The shaded portion below the Nyquist frequency u_N adds to the sampled NPS. Also depicted is white signal shot noise.

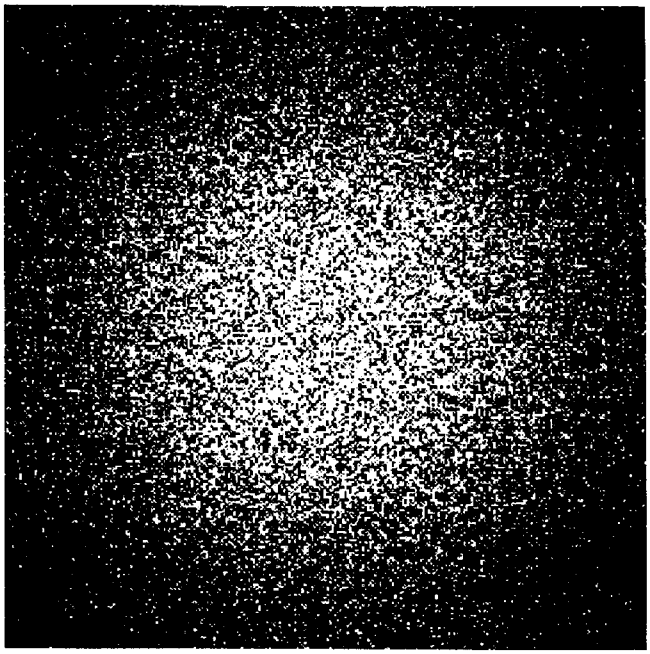

Fig. 15 Fourier amplitude spectrum of a homogeneous exposure recorded with an XRII/CCD-camera chain.

Finally, Fig. 16 shows DQE curves for a 400 μm CsI entrance screen, an entire 23 cm image intensifier equipped with such a screen, and a complete imaging chain with a 1 k×1 k CCD camera. The Nyquist frequency u_N of this system is 2.2 lp/mm. Below 2 lp/mm, the DQEs of both the XRII and the entire chain are almost exclusively determined by the CsI screen. Above 3 lp/mm, the XRII-DQE falls below the CsI DQE. This is a result of the increased weight of flat signal shot noise of the photoelectrons over lowpass-filtered quantum noise and signal for high frequencies. The rather steep drop of the DQE for the entire imaging chain between 2 lp/mm and the Nyquist frequency is caused by sampling and the aliased noise components shown in Fig. 14. Still, due to the absence of triangular noise, the DQE of a CCD-based imaging chain is much better than that one of a plumbicon-based chain. Thus, considerable MTF restoration is possible without introducing unacceptably high noise levels. As shown in Fig. 13, the total system MTF has fallen to about 0.2 at 2 lp/mm. Ac-

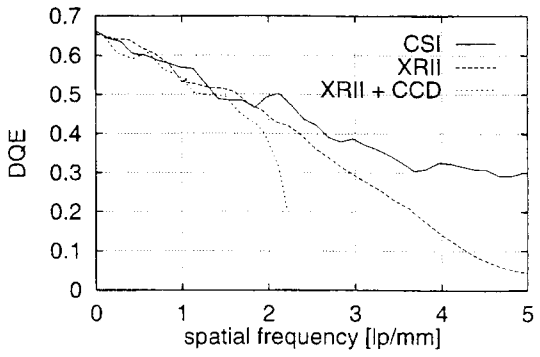

Fig. 16 DQE curves for 60 keV average beam energy of a CsI screen, an XRII, and a total imaging chain with a 1 k×1 k-pixel CCD camera.

cording to Eq. (8), and with DQE values of 0.65 at zero spatial frequency and 0.37 at 2 lp/mm, the MTF can be restored to about 0.75 at 2 lp/mm.

In summary, image quality can be improved with respect to three major points by the introduction of CCD cameras: first, the excellent geometrical stability of the sensor array improves modalities like subtraction angiography, where accurate *registration* of several images with respect to each other is important. This enables also better correction of fixed pattern noise. Second, the MTF of a CCD camera is considerably better than the MTF of a pickup tube. Due to the physical separation of pixels in a CCD, this holds also for low spatial frequencies. In a pickup tube, transfer of low spatial frequency information can be reduced by, among other effects, large-area equalization of the charge image on the target during readout. Third, the absence of triangular noise improves the SNR and DQE particularly for higher spatial frequencies, thus allowing a higher degree of digital MTF restoration and edge enhancement. To still keep quantization noise negligible compared to the reduced noise levels particularly at higher spatial frequencies, 12 bit A/D conversion may be advisable rather than the previously mentioned 8 or 10 bit conversion. Further advantages of a CCD camera include its low sensitivity to electromagnetic interferences, and a mechanical construction which is much more compact than that of pickup tubes.

4 Solid-State Large Area Flat Dynamic X-Ray Image Detector (FDXD)

Despite the excellent image quality today's XRII/TV-camera chains achieve, there are some drawbacks of these systems. One is the bulkiness, size and weight particularly of the XRII, which hampers especially bedside imaging with mobile fluoroscopy systems. Furthermore, the systems suffer from geometric distortion, veiling glare and vignetting. Veiling glare refers to disturbing light in the output images of an XRII caused by scatter of x-ray quanta, photoelectrons and light photons inside the XRII, which reduces contrast. Vignetting denotes the drop in output image intensity toward the circular image boundary, which is caused by the convex shape of the XRII input screen. Although both veiling glare and vignetting can be compensated digitally, it is preferable to prevent them in the first place.

This can be accomplished with an all solid-state image sensor which does not rely on electron and light-optical components and therefore promises negligible vignetting and veiling glare, zero geometric distortion due to its rigid pixel matrix, and a flat input screen. In addition the devices can be made compact and light-weight even for very large quadratic or rectangular field sizes up to 50×50 cm^2. With a pixel pitch about 100–200 μm, and a very large dynamic range, such a device is very well suited for high quality digital radiography. At the same time it can be used as a fluoroscopy imager using a readout mode with reduced pixel count, obtained by either zooming or pixel binning.

The fabrication of large area solid-state image sensors has now become feasible by the progress made in thin-film electronics technology which has been developed for flat displays. A detector array is realized by a 2D matrix of sensor elements as schematically depicted in Fig. 17. Each sensor element consists of an amorphous silicon (a-Si)

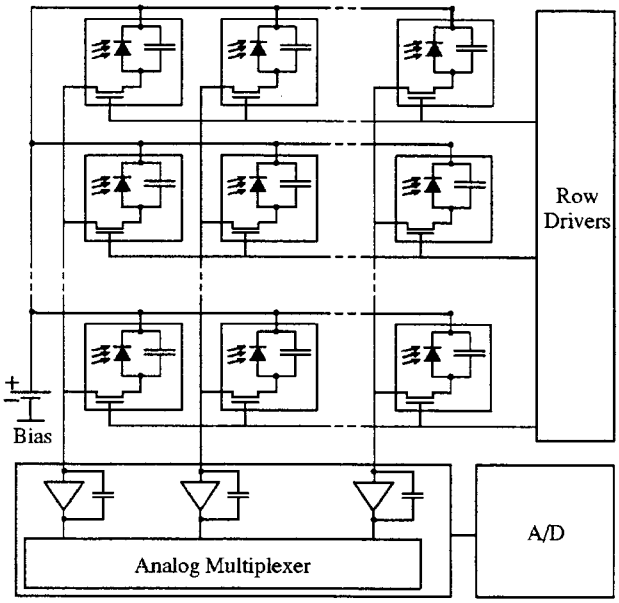

Fig. 17 Schematic of the solid-state detector.

photodiode and a thin-film transistor (TFT).[22] The array is covered by a thallium-doped CsI-scintillator screen making it sensitive to x radiation.[23]

The main issues we will address are signal transfer and detector noise. The results show that the SNR of the device can be made sufficiently large even at very low dose rates, despite the fact that there is no photoelectron amplification step involved.

4.1 *Structure of the Detector*

Figure 17 shows the detector setup: each pixel—formed by a photodiode and a TFT—is connected via a data line to a charge sensitive readout amplifier, and is linked by a gate line to a row driver. The photodiode sensitivity is spectrally matched to the thallium-doped CsI layer, i.e., is highest between 550 and 600 nm, where thallium-doped CsI light emission is strong. Via an analog multiplexer each readout amplifier is connected to an A/D converter. The charge generated after illuminating the detector is read out by successive activation of the detector rows via the row drivers. The charge of an activated row is transferred to the readout amplifiers, and subsequently digitized.

4.2 *Signal Transfer and Noise*

To analyze signal and noise behavior, we focus on fluoroscopy, which, due to the low doses used, is more critical than medium or high-dose radiography. The target is to achieve a fluoroscopy performance which is comparable or better than that of XRII/TV-camera chains. This means that especially for low doses electronic detector noise must be significantly lower than quantum noise, which, according to Sec. 2, is also low at low doses.

In order to present quantitative figures on SNR performance achieved so far, we consider a $1\text{ k}\times1\text{ k}$ pixel detector with 200 μm pitch and a corresponding Nyquist frequency of 2.5 lp/mm as described in Ref. 22.

Signal transfer is mainly characterized by the detector gain G quantifying the conversion of x radiation into elec-

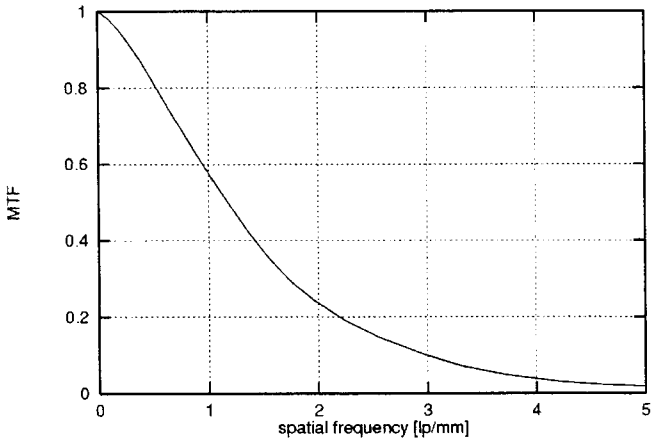

Fig. 18 Presampling MTF of the solid-state detector.

tron charge within each photodiode, and by the MTF. For a given, typical fluoroscopy x-ray beam quality, the gain is measured in electrons generated in each pixel per nGy of radiation incident on the array. With an optical reflector coating on top of the CsI screen, which prevents the escape of generated luminescence photons, values of $G = 700$ electrons/nGy were measured for a prototype detector in Ref. 22. In the meantime this value has been improved to about 1500 electrons/nGy by increasing the active size of the photodiodes and by optimizing the CsI deposition process.[23]

The presampling MTF for the analog detector components before sampling, i.e., the CsI screen and the finite pixel pitch, is shown in Fig. 18. As the presampling MTF does not vanish beyond the Nyquist frequency, some aliasing of quantum noise will occur, similarly as described for CCD sensors in Sec. 3.4. With the MTF at Nyquist frequency having dropped to approximately 15%, the influence of aliased noise is appreciable but not too severe.

The main electronic noise sources of this detector are the readout amplifier noise and the reset noise of the pixel capacitances. In order to relate the noise measurements to the signal level, the noise standard deviation is in the following also expressed in electrons, and refers to a single pixel.

The effective amplifier noise depends on the readout timing pattern. Our prototype is read out by so-called *correlated double sampling* (CDS) depicted in Fig. 19.[22] The gate of each TFT in a row is activated by the corresponding row driver through a positive pulse, which enables flow of the signal charge to the readout amplifier. To avoid distortion of the sampled charge signal by additional charge fed capacitively through the TFT gate during the positive slope of the activation pulse, sampling of the amplified charge signal occurs only after the TFTs are deactivated again, i.e., after the capacitive feedthrough has been reversed by the negative slope of the activation pulse. From this sample, another sample is subtracted which was taken *before* charge readout. This readout timing scheme acts as a highpass filter which efficiently suppresses offsets and a lowpass noise component of the amplifiers, which is known as $1/f$ noise. Simultaneously, the finite sampling aperture of about 8 μs acts as a lowpass filter attenuating white amplifier noise.

With this timing scheme the pixel capacitances' noise is given by $\sqrt{2kTC_p}$, where T is the absolute temperature, k the Boltzmann constant, and C_p the pixel capacitance which is typically on the order of 2 pF.

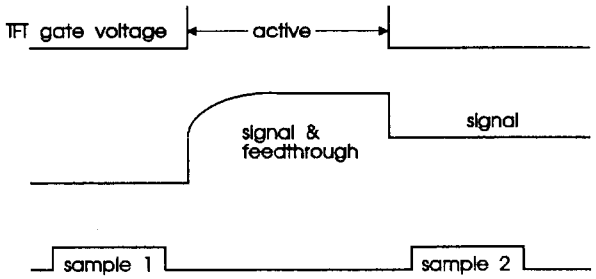

Fig. 19 Timing of correlated double sampling. Sample 1 taken before readout is subtracted from sample 2 which is taken after capacitive feedthrough has been reversed. The sampling aperture is about 8 μs.

4.2.1 *Fluoroscopy performance*

Let us now examine the potential signal-to-noise performance of a 1 k×1 k-pixel array with 200 μm pitch at a typical fluoroscopic dose rate of 10 nGy/frame and an average beam energy of 60 keV. At a gain G of 1500 electrons/nGy, this generates a signal of 15 000 electrons per pixel. With $q_0 = 300$ quanta/mm^2, the number of x-ray quanta Q absorbed per pixel is about 10. Hence, after detection the standard deviation of x-ray quantum noise per pixel is given by $G\sqrt{Q} = 4740$ electrons.

When using correlated double sampling, the standard deviation of readout amplifier noise is about 600 electrons. The pixel capacitances' noise is about 800 electrons. These figures result in an overall electronic noise with a standard deviation of 1000 electrons.

Hence the SNR of the detector is clearly determined by quantum noise at typical fluoroscopic dose rates. Even in dark image areas, where quantum counts are as low as one per pixel, the quantum noise still is at 1500 electrons, exceeding the overall electronic noise.

Assuming a pixel size of 200×200 μm^2, the corresponding values for XRII/TV-camera chains are a gain of about 10 000 electrons per 10 nGy and pixel, at an electronic noise level of approximately 200 electrons. These figures show that the electronic SNR performance of XRII/TV-camera systems will not quite be reached by the solid-state detector, but the difference should in practice be insignificant, due to the dominant x-ray quantum noise. In addition for the solid-state detector the absorption efficiency for the x-ray quanta can be further increased, hence increasing the overall SNR for a given entrance dose.

4.3 *Digital Processing*

To achieve optimal detector performance, it is necessary to compensate fixed pattern effects like variations in offset and gain of the sensor elements by suitable digital processing. An additional effect which should be corrected digitally is the *memory effect*, which denotes the remaining of an undesired residual image after image readout. This is caused by the incomplete flowing off of electrons from the photodiodes. The memory effect is intrinsic to amorphous

silicon, and can be described by an appropriate model.[24] Based on this model, digital compensation of the memory effect is feasible.

In conclusion, when taking into account the above-mentioned advantages of the solid-state detector of no geometric distortion, no veiling glare, and no vignetting, we expect that the overall image quality of these future x-ray imagers will be superior, provided that the best performance achieved in laboratory models so far can be transferred to the production of clinical imaging devices.

5 Digital Quantum Noise Reduction

Regardless of whether one employs the described solid-state detector or the discussed XRII/TV-camera chain, fluoroscopy images are always afflicted by relatively high quantum noise levels compared to signal due to the low dose rates used. One possibility to reduce quantum noise in the observed images is by appropriate digital noise filtering. In full frame rate fluoroscopy with 25 or more images per second, this can be done by recursive temporal averaging, what can be interpreted as digitally introducing an intended lag. To prevent blurring of moving objects, filtering is reduced or switched off entirely in areas where object motion is detected (*motion adaptive filtering*).[25,26]

For low frame rate fluoroscopy mentioned in Sec. 3.1, however, temporal filtering is often not feasible, so that the only option which remains is spatial filtering within single images. Such an algorithm is described in the following.

To reduce noise, the filtering algorithm has to exploit structural differences between signal content of images and noise. Modelling of noise can be based on our previous discussions in Secs. 2 and 3. However, appropriate modeling of the signal content of medical images is difficult if not impossible. The often used Markov random field models, for example, do not capture sufficient medical detail if kept mathematically tractable. It is therefore desirable to keep the assumptions on the signal as weak as possible. We hence rely here on a noise model as starting point and assume those input observations as containing image signal (in addition to noise) that cannot be explained well by noise only.

5.1 *Noise Reduction by Spectral Amplitude Estimation*

We have already seen that quantum noise exhibits a lowpass-shaped power spectrum in the acquired images. A relatively high proportion of the overall noise power is hence contributed from low spatial frequencies. Standard spatial window-based filters, like lowpass convolution kernels, nonstationary Wiener approaches,[27] or order statistic-based filters,[28–30] however, tend to attenuate mainly high spatial frequency components. This has the twofold shortcoming that, first, the full noise reduction potential is not exploited. Second, the filtering operation shifts the spectral composition of quantum noise even more towards low spatial frequencies, what is often visually unpleasing despite a reduction of the overall noise power. Additionally, order statistic-based filters tend to generate patches or streaks of constant intensity,[30,31] which add to the unnatural appearance of such processed images.

To avoid such artifacts without sacrificing noise reduction performance, and in particular to be able to tailor our filters to spatially coloured noise, we apply here the concept of so-called *spectral amplitude estimation*, where noise attenuation is carried out in the spectral domain.[32] Spectral amplitude estimation is a widely reported approach to speech restoration,[33–36] but there are only few reported image processing applications.[37] Starting with a decomposition of the input images into overlapping blocks which are subjected to a standard block transform [discrete fourier transform (DFT) or discrete cosine transform (DCT)], the central idea is to compare each transform coefficient to the corresponding "noise only" expectation, i.e., to its counterpart from the NPS. Each coefficient is then attenuated depending on how likely it is that it contains only noise. The purpose of the block decomposition is to make the filter algorithm adaptive to small image detail as well as to nonstationarities of noise.

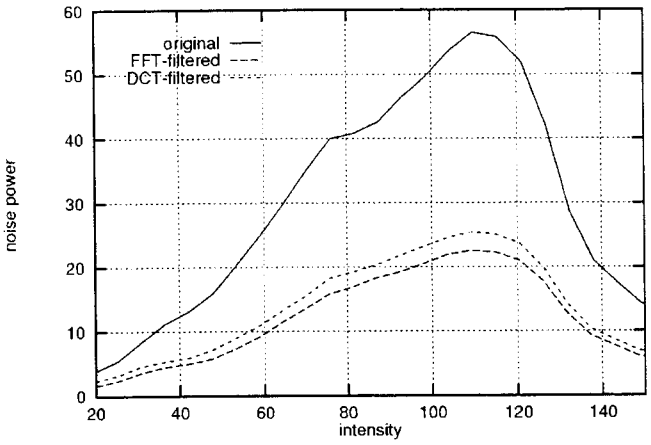

Fig. 20 Noise power vs signal intensity for the fluoroscopy sequence in Fig. 10. Also shown is the noise power which remains after filtering by DFT- and DCT-based spectral amplitude estimation was applied.

5.1.1 *Quantum noise model*

We have already seen that, due to its Poissonian nature, the quantum noise power depends linearly on the quantum flow q_0, that is, on signal. For the digitized fluoroscopy image shown in Fig. 10, this dependence over image intensity is depicted in Fig. 20. Over low to medium intensities, this curve exhibits (approximately) the predicted linear rise. The drop-off toward high intensities is caused by the reduced amplifier gain for high signal amplitudes (white compression, Sec. 3.2). Second, as already discussed and shown in, e.g., Fig. 15, quantum noise exhibits a lowpass shaped power spectrum in the acquired images. For a given fluoroscopy system, both the signal dependence and the NPS of quantum noise are assumed to be known. Furthermore, we assume that quantum noise is the dominating noise source (*quantum-limited imaging*), and that the system MTF is signal independent. Signal dependence of quantum noise then affects only the absolute *scale* of the NPS, but not its *shape*. We therefore separate signal dependence and spatial frequency dependence of the observed NPS $N^2(S,u)$ by

$$N^2(S,u)=\sigma^2(S)n^2(u), \tag{9}$$

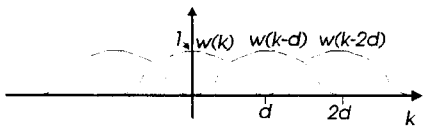

Fig. 21 1D illustration of the use of overlapping windowed blocks over a spatial coordinate k to prevent blocking artifacts in processed images. The periodically repeated window function $w(k)$ adds up to unity, thus allowing perfect reconstruction of the original image. If the DFT is used, windowing serves the double function of allowing block overlaps and preventing leakage.

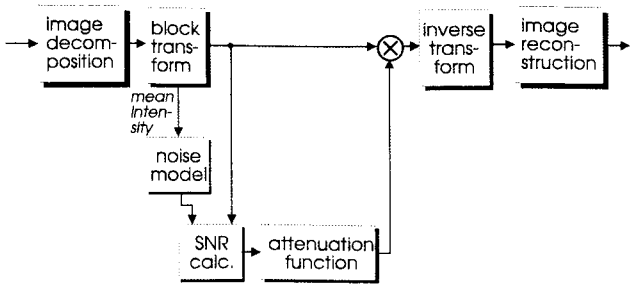

Fig. 22 Block diagram of the spectral amplitude estimation filter for noise reduction.

where $\sigma^2(S)$ is the noise power which depends on signal S as illustrated in, e.g., Fig. 20. The spatial frequency dependence or NPS shape is captured by the reference NPS $n^2(u)$, which integrates to unity.

As our spectral amplitude estimation filter is based on block transforms like DFT or DCT, we estimate the NPS by well-known periodogram averaging techniques based on the same block size and analysis window type as the one used later in the noise reduction algorithm. For a given system, the described estimation is done *a priori* from homogeneous exposures like the ones used for Figs. 12 and 15. Windowing serves here the double purpose of preventing DFT leakage and enabling the use of overlapping blocks in order to avoid blocking artifacts in the processed images (see Fig. 21). Signal dependence $\sigma^2(S)$ and the NPS shape $n^2(u)$ are stored in look-up tables.

5.1.2 *Spectral amplitude estimation filter*

In the following, we denote the observed, noisy spectral coefficients by $Y(u)$. To compare these observations to what we would expect if only noise were present, we calculate the so-called *instantaneous* SNR $r(u)$, which relates the *instantaneous* power of each observation $Y(u)$ to the *expected* noise power $\Phi(u)$. The squared instantaneous SNR is given by

$$r^2(u)=\frac{|Y(u)|^2}{\Phi(u)}, \tag{10}$$

where (an estimate for) $\Phi(u)$ is easily obtained from the NPS in Eq. (9): estimation of the NPS by periodogram averaging involves normalization by the squaresum of window coefficients.[37,38] Simply dropping this normalization yields the desired estimate for $\Phi(u)$. Noise reduction is achieved by attenuating each observation $Y(u)$ depending on $r^2(u)$ according to

$$\hat{S}(u)=Y(u)h(r(u)). \tag{11}$$

The *attenuation function* $h(r)$ varies between zero and one, and increases monotonically over r. The total effect is an attenuation of spectral coefficients which are likely to represent mainly noise. Generally, the attenuation function is real valued. Equation (11) therefore is a zero-phase filter, hence the name *spectral amplitude estimation.*

Figure 22 shows the block diagram of the noise filter. The box termed "noise model" stores the signal dependence of quantum noise and the reference NPS of Eq. (9). After image decomposition and DFT, the corresponding NPS coefficient $N^2(S,u)$ for each observation is read out from this box, where the mean block gray level $Y(0)$ is used as an estimate for the signal intensity S needed to access the appropriate scaling factor [we make here the approximating assumption that the signal-dependent noise is stationary within a block (short space stationarity)]. $\sigma^2(S)$. The SNR $r(u)$ can now be calculated, and the corresponding attenuation factor $h[r(u)]$ is read out from the "attenuation function" box. $Y(u)$ is then multiplied by $h[r(u)]$, before the noise reduced image is reconstructed by taking the inverse DFT, and reassembling the image blocks.

The precise shape of the attenuation function is determined by the chosen objective function and the underlying models for noise and signal.[34,37,39,40] Our filter algorithm is based on the concept of minimum mean square error estimation of spectral amplitudes.[32] The resulting attenuation function is derived in Appendix B, and depicted in Fig. 23.

5.2 *Processing Results*

Figure 24 shows the enlarged central portion of the fluoroscopy image in Fig. 10, and the filtered version is depicted in Fig. 25. This result was obtained using the DFT in connection with a blocksize of 64×64 pixel and an overlap of 16 pixel. The DFT window was a modified separable 2D

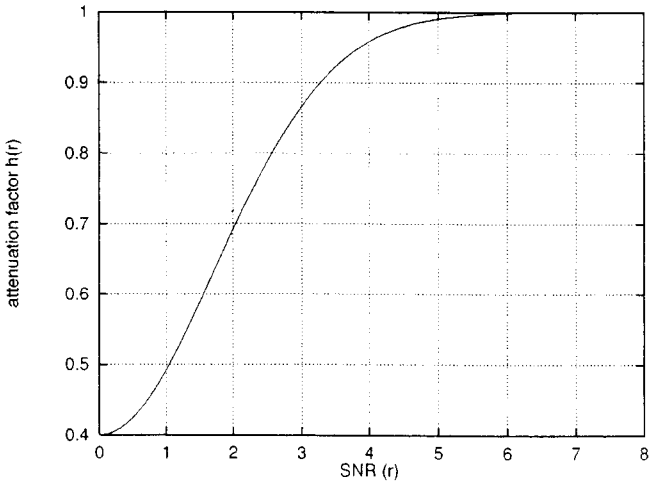

Fig. 23 Attenuation h as function of the instantaneous SNR r, derived based on the concept of minimum mean square error estimation.

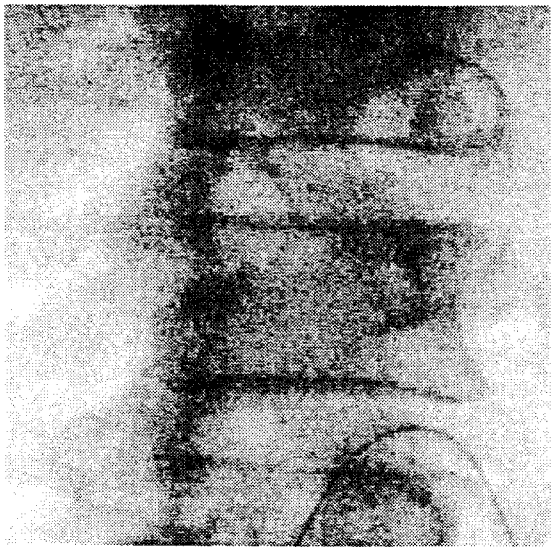

Fig. 24 Enlarged portion of the image in Fig. 10.

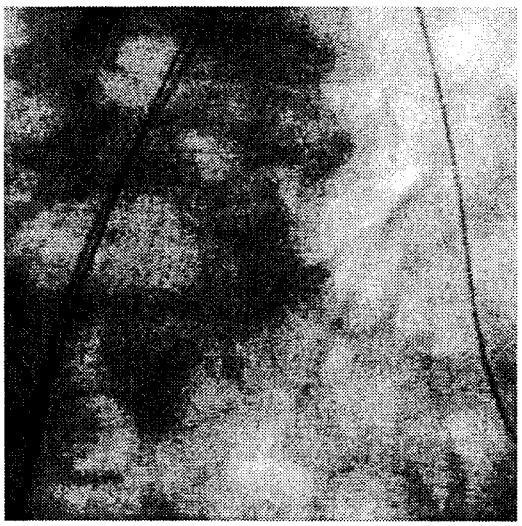

Fig. 26 Part of a low dose x-ray image, showing a thin guidewire inserted into a patient's vascular system.

Hanning window, whose cosine-shaped drop-off was restricted to a 16 pixel wide border region. The noise power remaining after filtering is still signal dependent, and quantitatively evaluated in Fig. 20, showing a noise power reduction by about 60%.

DCT based processing results are hardly distinguishable from those obtained using DFT. As shown in Fig. 20, quantitative noise reduction performance is also similar to the DFT-based processing. One advantage of the DCT is its negligible leakage. Windowing before taking the transform can hence be omitted. Block overlap is now only necessary to avoid the block raster from becoming visible, what can be ensured by overlaps as low as two pixels, reducing the computational load by about 40%. The window operation required by block overlap is now performed within the image reconstruction box in Fig. 22.

A processing result for another image (Fig. 26) is shown in Fig. 27. This result was obtained by a modified spectral amplitude estimation algorithm which explicitly detects and exploits perceptually important oriented structures, like guide wires, catheters, or edges of bones.[41] When using the DFT, the occurrence of an oriented structure in an image block results in the spectral domain in a concentration of energy along the line perpendicular to the spatial orientation and passing through the origin. For each image block, our modified algorithm uses an inertia matrix-based method to detect the line along which concentration of energy is strongest.[41,42] The filter then explicitly adapts to the detected orientation by applying less attenuation to—or by even enhancing—coefficients along this line, with this behavior being the more pronounced, the more distinct the local orientation.[41] Correspondingly, the processed image shows both strong suppression of noise and enhancement of lines and edges, like the guide wire. Another example of a fluoroscopy image is shown in Fig. 28, and the processing result in Fig. 29. Unlike the previous image, this example

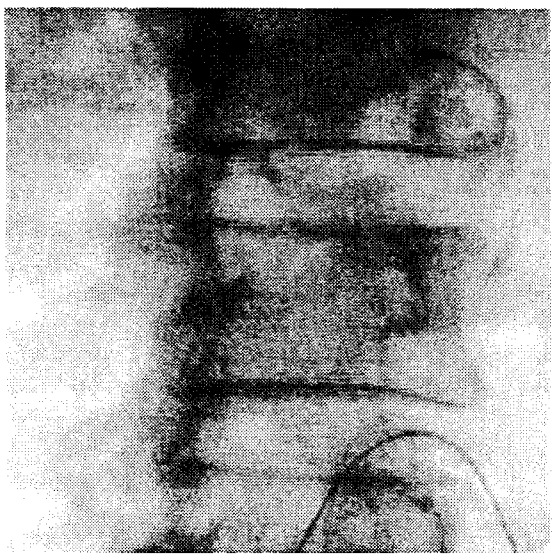

Fig. 25 Noise-reduced version of Fig. 24.

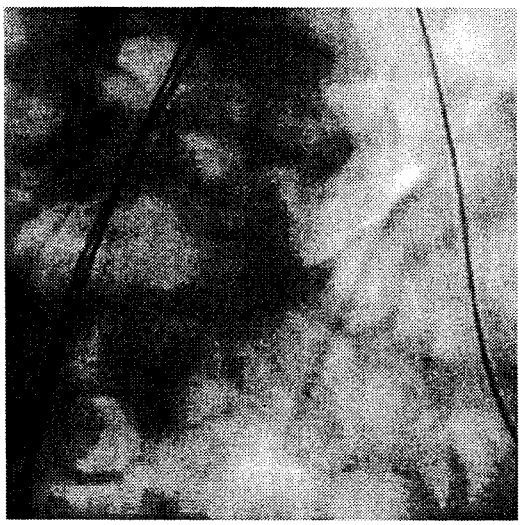

Fig. 27 Figure 26 processed by orientation-dependent noise reduction and enhancement.

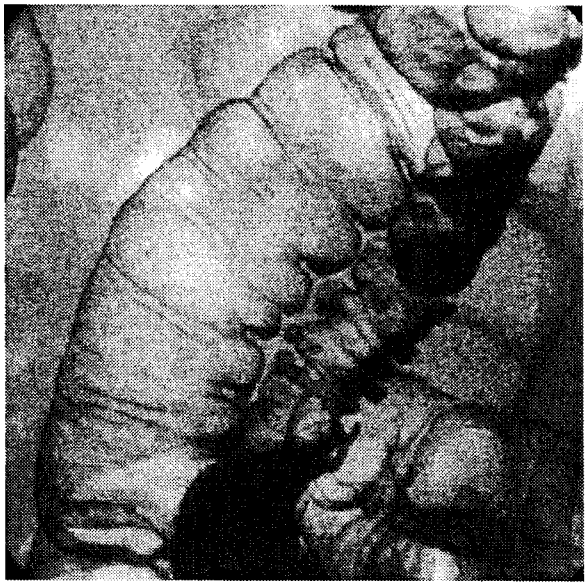

Fig. 28 Part of a fluoroscopy image depicting intestines.

contains no sharp guide wires, but is dominated by medium-sharp anatomic structures like fissures and the transition from intestines to background, which are also enhanced.

To relate the achieved noise power reduction to potential degradations of the MTF during filtering, we have also measured the SNR before and after filtering. Our filter being adaptive implies, of course, that its performance is dependent on the input signal. For our measurements, we simulated different versions of a "difficult" image of a thin guidewire embedded in quantum noise, corresponding to acquisitions at 10, 30, and 100 nGy, respectively. For each simulated acquisition dose, the ratio of the SNR after filtering to the SNR before filtering is depicted over spatial frequency in Fig. 30. [Loosely speaking, this ratio could be

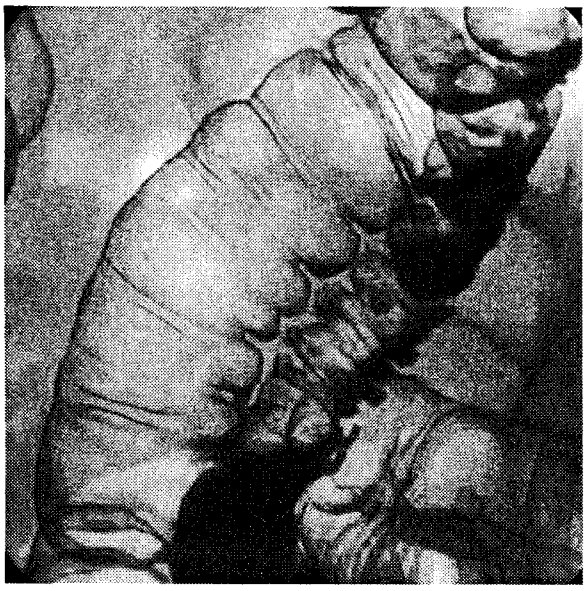

Fig. 29 Figure 28 processed by orientation-dependent noise reduction and enhancement.

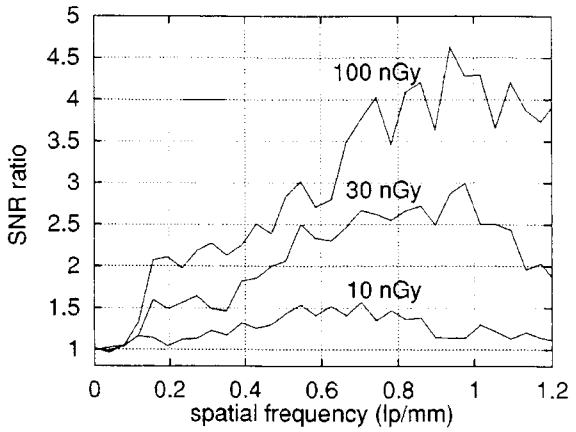

Fig. 30 Ratio of SNR after processing to SNR before processing as a function of spatial frequency. Measurements based on 30 realizations of a simulated test image containing a thin guidewire and quantum noise corresponding to acquisitions at 10, 30, and 100 nGy.

interpreted as a (signal dependent) DQE of the filter.] The measurements were based on 30 realizations of each test image. Evidently, the SNR is indeed improved over a wide range of spatial frequencies, i.e., potential losses of MTF are outweighed by the reduction of noise power.

5.3 *Discussion*

The strength of our spectral domain approach to quantum noise reduction is that it can be tailored specifically to the known properties of quantum noise, while only very general assumptions about the behavior of the unknown signal under orthogonal transforms are required.

It might appear as a shortcoming of the discussed algorithms that processing is based on an unnatural block structure. In the present context, however, blockwise processing has the significant advantage that inevitable "decision" errors, especially mistaking noise for signal, are dispersed over entire blocks as sine-like gratings. The occasional appearance of these gratings can easily be concealed by retaining a low wideband noise floor. The visually much more unpleasing patch-like artifacts of spatial domain filters are thus completely avoided. The block raster itself is prevented from becoming visible through the use of overlapping blocks. The advantage of the DCT-based filter is that it keeps the computational overhead to a minimum, whereas the DFT provides a framework well suited for the exploitation of local orientation.

6 Concluding Remarks

This article described selected topics of medical x-ray image acquisition and processing by digital techniques, some of which are already well established, while others are presently emerging. By first comparing digital radiography systems to analog ones, it was shown that a key advantage of digital imaging lies in the inherent separation of image acquisition and display media, which enables one to digitally restore and enhance acquired images before they are displayed. It turned out that the amount of restoration and enhancement which can be applied is fundamentally limited by noise. The performance of digital imaging systems was therefore characterized by the signal-to-noise ratio and

related measures. Expressing the SNR in terms of x-ray quantum flow resulted in the two principal performance measures, viz., noise equivalent quanta (NEQ) and detective quantum efficiency (DQE). Essentially, these measures quantify how effectively the incoming quantum flow is exploited by an imaging system at different spatial frequencies.

The relation between signal and noise transfer was emphasized in our subsequent discussions, starting with present-day fluoroscopy systems based on x-ray image intensifier/camera chains. We highlighted the fundamental differences in noise behavior between vacuum camera tubes and CCD cameras, and discussed the major points where image quality can be improved by the introduction of CCD cameras. We then presented a concept for a flat solid-state x-ray detector based on amorphous silicon, which is intended to be used for both high resolution radiography and fluoroscopy. Here, we analyzed signal transfer and noise properties for the more critical application to low-dose fluoroscopy and showed that this concept can indeed be a viable alternative to XRII/TV systems. Present development efforts, however, focus on the introduction of this and other flat detector types into the market for digital radiography.[43,44] Other flat detector types include a-Si detectors with direct diode switching without using TFTs,[45,46] and detectors using amorphous selenium (a-Se) to detect x radiation, which are read out by TFT matrices.[47,48] Finally, we described a new noise reduction algorithm specifically tailored to the reduction of x-ray quantum noise in low-dose x-ray images, where the SNR is especially low. As a purely spatial filter, this algorithm is particularly suited for low frame rates often used in connection with pulsed fluoroscopy, where temporal filtering is often not feasible.

Appendix A

To see that the power spectral density N_q^2 of quantum noise is given by the quantum flow q_0, consider an ideal detector which counts quanta impinging on an area A. The detected signal then obeys $S=q_0A$. Due to the Poissonian nature of quantum noise, S is also identical to the noise power σ^2 at the detector output. The impulse response $f(x)$ of this detector is

$$f(x)=\begin{cases}1 & \text{if } x\in A,\\ 0 & \text{else,}\end{cases} \tag{A1}$$

where x is the spatial coordinate. The noise power can also be calculated from

$$\sigma^2=N_q^2\int_{-\infty}^{\infty}f^2(x)dx=N_q^2A. \tag{A2}$$

Hence, $N_q^2=q_0$.

Appendix B

The MMSE estimate $\hat{S}(u)$ of the noise-free spectral coefficient $S(u)$ is given by the conditional mean $\hat{S}(u)=E[S(u)|Y(u)]$, and explicitly exploits the well-known signal energy compaction properties of both the DFT and the DCT. Assuming for each block that the undistorted image signal appears in only a few coefficients, each observed coefficient represents either noise only (null hypothesis H_0), or signal and noise (alternative hypothesis H_1). Splitting up $E[S(u)|Y(u)]$ according to these hypotheses, we clearly have $E[S(u)|Y(u),H_0]=0$. The conditional mean can then be rewritten to

$$\begin{aligned}\hat{S}(u)&=E[S(u)|Y(u)]\\&=E[S(u)|Y(u),H_1]\cdot(1-\Pr[H_0|Y(u)]),\end{aligned} \tag{B1}$$

where $\Pr[H_0|Y(u)]$ is the probability for the null hypothesis given $Y(u)$. Furthermore, based on the single observation $Y(u)$ corrupted by zero-mean noise, and with no further prior knowledge available, we have $E[S(u)|Y(u),H_1]=Y(u)$. Using the Bayes rule, $\Pr[H_0|Y(u)]$ can be rewritten to

$$\Pr[H_0|Y(u)]=\frac{p[Y(u)|H_0]\cdot\Pr(H_0)}{p[Y(u)]}, \tag{B2}$$

with $p[Y(u)|H_0]$ denoting the probability density function (pdf) for the noisy observation when signal is absent. The unconditional pdf $p[Y(u)]$ can be split up into

$$\begin{aligned}p[Y(u)]&=p[Y(u)|H_0]\Pr(H_0)\\&\quad+p[Y(u)|H_1]\cdot(1-\Pr(H_0)).\end{aligned} \tag{B3}$$

Equation (B1) can now be rewritten to

$$\hat{S}(u)=Y(u)\left[1+\frac{p[Y(u)|H_0]\cdot\Pr(H_0)}{p[Y(u)|H_1]\cdot\Pr(H_1)}\right]^{(-1)}. \tag{B4}$$

Since each spectral coefficient is a weighted sum of the gray levels in the processed block, we assume the coefficients as complex Gaussian distributed according to the central limit theorem. For the null hypothesis, i.e., when the observation $Y(u)$ is caused by noise only, this complex Gaussian pdf is given by

$$p[Y(u)|H_0]=\frac{1}{\pi\Phi(u)}\exp\left\{-\frac{|Y(u)|^2}{\Phi(u)}\right\}, \tag{B5}$$

where $\Phi(u)$ is the noise variance defined in Sec. 5.1. For $Y(u)$ given hypothesis H_1, i.e., when signal is present, another complex Gaussian pdf can be assumed with unknown variance. Typically, however, the variance $P(u)$ of coefficients containing both signal and noise is much larger than $\Phi(u)$. Inserting the complex Gaussian pdfs into Eq. (B4), the following expression for the estimate can then be derived:

$$\hat{S}(u)=Y(u)\left(1+\lambda\exp\left\{-\frac{|Y(u)|^2}{\Phi(u)}\right\}\right)^{-1}, \tag{B6}$$

with

$$\lambda = \frac{P(u)\Pr(H_0)}{\Phi(u)\Pr(H_1)}. \tag{B7}$$

Finally, we introduce a weighting factor α for the noise variance, similarly as done in, e.g., generalized Wiener filters.[49] We then obtain

$$\hat{S}(u) = Y(u)\left(1 + \lambda \exp\left\{-\frac{r^2(u)}{\alpha}\right\}\right)^{-1} = Y(u)h[r(u)], \tag{B8}$$

where $r(u)$ is the instantaneous SNR of Eq. (10), and $h[r(u)]$ the MMSE attenuation function. The quantity λ is the (noninstantaneous) signal-plus-noise to noise ratio weighted by $\Pr(H_0)/\Pr(H_1)$. As the precise values of $P(u)$, $\Pr(H_0)$ and $\Pr(H_1)$ are unknown, we regard λ as a free parameter to be selected externally, similarly as done, e.g., with regularization parameters in regularized image processing paradigms. Experimentally, we found that $\lambda = 1.5$ and $\alpha = 3.0$ gave good processing results. The corresponding attenuation function is depicted in Fig. 23.

Acknowledgments

This work was performed while all authors were with Philips Research Laboratories, Aachen, Germany. We thank M. Weibrecht and C. Mayntz for fruitful discussions.

References

1. D. Meyer-Ebrecht, "The filmless radiology department—A challenge for the introduction of image processing into medical routine work," in *4th IEE International Conference on Image Processing and its Applications*, Maastricht, NL (April 1992).
2. M. Ishida, "Image Processing," in *Computed Radiography*, Y. Tateno, T. Iinuma, and M. Takano, Eds., pp. 25–30, Springer-Verlag, Berlin (1987).
3. W. Hillen, U. Schiebel, and T. Zaengel, "Imaging performance of a digital storage phosphor system," *Med. Phys.* **14**(5), 744–751 (1987).
4. A. R. Cowen, A. Workman, and J. S. Price, "Physical aspects of photostimulable phosphor computed radiography," *Br. J. Radiol.* **66**, 332–345 (1993).
5. U. Neitzel, I. Maack, and S. Günther-Kohfahl, "Image quality of a digital chest radiography system based on a selenium detector," *Med. Phys.* **21**(4), 509–516 (1994).
6. W. Hillen, S. Rupp, U. Schiebel, and T. Zaengel, "Imaging performance of a selenium-based detector for high-resolution radiography," in *Medical Imaging III: Image Formation, Proc. SPIE* **1090**, 296–305 (1989).
7. A. R. Cowen, A. Giles, A. G. Davies, and A. Workman, "An image processing algorithm for PPCR imaging," in *Image Processing, Proc. SPIE* **1898**, 833–843 (1993).
8. A. G. Davies, A. R. Cowen, G. J. S. Parkin, and R. F. Bury, "Optimising the processing and presentation of PPCR images," in *Medical Imaging 1996: Image Perception, Proc. SPIE* **2712**, 189–195 (1996).
9. I. Maack and U. Neitzel, "Optimized image processing for routine digital radiography," in *Proceedings of the Computer Assisted Radiology (CAR 91)*, U. Lemke, Ed., pp. 108–114, Springer-Verlag, Berlin (1991).
10. S. Ranganath and H. Blume, "Hierarchical image decomposition and filtering using the S-transform," in *Medical Imaging II, Proc. SPIE* **914**, 799–814 (1988).
11. ICRU, "Medical imaging—the assessment of image quality," Report No. 54, International Commission on Radiation Units and Measurements (1996).
12. A. L. Evans, *The Evaluation of Medical Images*, Adam Hilger, Bristol (1981).
13. R. Shaw, "The equivalent quantum efficiency of the photographic process," *J. Photographic Sci.* **11**, 199–204 (1963).
14. J. C. Dainty and R. Shaw, *Image Science*, Academic, London (1974).
15. M. Rabbani, R. Shaw, and R. van Metter, "Detective quantum efficiency of imaging systems with amplifying and scattering mechanisms," *J. Opt. Soc. Am. A* **4**(5), 895–901 (1987).
16. H. Blume, J. Colditz, W. Eckenbach, P. t'Hoen, J. Meijer, T. Poorter, R. M. Snoeren, W. E. Spaak, and G. Spekowius, "Image intensifier and x-ray exposure control systems," *RSNA Categorical Course in Physics*, pp. 87–103 (1995).
17. G. Spekowius, H. Boerner, W. Eckenbach, P. Quadflieg, and G. J. Laurenssen, "Simulation of the imaging performance of x-ray image intensifier/TV camera chains," in *Medical Imaging 1995, Proc. SPIE* **2432**, 12–23 (1995).
18. W. Hillen, W. Eckenbach, P. Quadflieg, and T. Zaengel, "Signal-to-noise performance in cesium iodide x-ray fluoroscopic imaging," in *Medical Imaging V: Image Physics, Proc. SPIE* **1443**, 120–131 (1991).
19. F. W. Schreiber, *Fundamentals of Electronic Imaging Systems*, Springer-Verlag, Berlin (1986).
20. G. Murphy, W. Bitler, J. Coffin, and R. Langdon, "Lag vs. noise in fluoroscopic imaging," in *Physics of Medical Imaging, Proc. SPIE* **1896**, 174–179 (1993).
21. C. H. Slump, "On the restoration of noise aliasing and moiré distortion in CCD-based diagnostic x-ray imaging," in *Medical Imaging VI: Image Processing, Proc. SPIE* **1652**, 451–462 (1992).
22. U. Schiebel, N. Conrads, N. Jung, M. Weibrecht, H. Wieczorek, T. Zaengel, M. J. Powell, I. D. French, and C. Glasse, "Fluoroscopic imaging with amorphous silicon thin-film arrays," in *Physics of Medical Imaging, Proc. SPIE* **2163**, 129–140 (1994).
23. H. Wieczorek, G. Frings, P. Quadflieg, U. Schiebel, T. Bergen, F. M. Dreesen, M. A. C. Ligtenberg, and T. Poorter, "CsI:Tl for solid state x-ray detectors," in *Proceedings of the International Conference on Inorganic Scintillators and their Applications (SCINT 95)*, C. W. E. v. E. P. Dorenbos, Ed., pp. 547–554, Delft (1995).
24. H. Wieczorek, "Measurement and simulation of the dynamic performance of *a*-Si:H image sensors," *J. Non-Cryst. Solids* **164–166**, 781–784 (1993).
25. J. C. Brailean, R. P. Kleihorst, S. Efstratiadis, A. K. Katsaggelos, and R. L. Lagendijk, "Noise reduction for dynamic image sequences: A review," *Proc. IEEE* **83**(9), 1272–1291 (1995).
26. T. Aach and D. Kunz, "Bayesian motion estimation for temporally recursive noise reduction in X-ray fluoroscopy," *Philips J. Res.* **51**(2), 231–251 (1998).
27. D. T. Kuan, A. A. Sawchuk, T. C. Strand, and P. Chavell, "Adaptive noise smoothing filter for images with signal-dependent noise," *IEEE Trans. Pattern. Anal. Mach. Intell.* **7**(2), 165–177 (1985).
28. A. Nieminen, P. Heinonen, and Y. Neuvo, "A new class of detail-preserving filters for image processing," *IEEE Trans. Pattern. Anal. Mach. Intell.* **9**(1), 74–90 (1987).
29. Y. S. Fong, C. A. Pomalaza-Ráez, and X. H. Wang, "Comparison study of nonlinear filters in image processing applications," *Opt. Eng. (Bellingham)* **28**(7), 749–760 (1989).
30. I. Pitas and A. N. Venetsanopoulos, "Order statistics in digital image processing," *Proc. IEEE* **80**(12), 1892–1921 (1992).
31. A. C. Bovik, "Streaking in median filtered images," *IEEE Trans. Acoust., Speech, Signal Process.* **35**, 493–503 (1987).
32. T. Aach and D. Kunz, "Spectral estimation filters for noise reduction in x-ray fluoroscopy imaging," in *Proc. EUSIPCO-96*, G. Ramponi, G. L. Sicuranza, S. Carrato, and S. Marsi, Eds., pp. 571–574, Edizioni LINT, Trieste (1996).
33. P. Vary, "Noise suppression by spectral magnitude estimation—mechanism and limits," *Signal Process* **8**(4), 387–400 (1985).
34. J. S. Lim and A. V. Oppenheim, "Enhancement and bandwidth compression of noisy speech," *Proc. IEEE* **67**(12), 1586–1604 (1979).
35. T. Aach and D. Kunz, "X-ray image restoration by spectral amplitude estimation as an extension of a speech enhancement approach," in *Proc. Aachener Symposium on Signal Theory*, B. Hill, M. Junggeburth, and F. W. Vorhagen, Eds., pp. 81–86, Institut f. Techn. Elektronik, RWTH Aachen (1997).
36. T. Aach and D. Kunz, "Spectral amplitude estimation-based X-ray image restoration: An extension of a speech enhancement approach," in *Proc. EUSIPCO-98*, S. Theodoridis, I. Pitas, A. Stouraitis, and N. Kalouptsidis, Eds., pp. 323–326, Typorama, Patras, Island of Rhodes, 5–9 Sept. 1998.
37. J. S. Lim, "Image restoration by short space spectral subtraction," *IEEE Trans. Acoust., Speech, Signal Process.* **28**(2), 191–197 (1980).
38. P. D. Welch, "The use of fast Fourier transform for the estimation of power spectra: A method based on time averaging short, modified periodograms," *IEEE Trans. Appl. Supercond.* **AU-15**(2), 70–73 (1967).
39. Y. Ephraim and D. Malah, "Speech enhancement using a minimum mean-square error short-time spectral amplitude estimator," *IEEE Trans. Acoust., Speech, Signal Process.* **32**(6), 1109–1121 (1984).
40. R. J. McAulay and M. L. Malpass, "Speech enhancement using a soft-decision noise suppression filter," *IEEE Trans. Acoust., Speech, Signal Process.* **28**(2), 137–145 (1980).
41. T. Aach and D. Kunz, "Anisotropic spectral magnitude estimation filters for noise reduction and image enhancement," in *Proceedings of the IEEE International Conference on Image Processing (ICIP-96)*, pp. 335–338, Lausanne (1996).
42. J. Bigün and G. H. Granlund, "Optimal orientation detection of linear symmetry," in *Proceedings of the IEEE First International Conference on Computer Vision*, pp. 433–438, London (1987).

43. "Digital x-ray capture," in *Supplement to: Diagnostic Imaging*, D3–D25 (Nov. 1996).
44. "On the horizon: Digital radiography," in *Med. Imaging*, 100–107 (Nov. 1996).
45. J. Chabbal, C. Chaussat, T. Ducourant, L. Fritsch, J. Michailos, V. Spinnler, G. Vieux, M. Arques, G. Hahm, M. Hoheisel, H. Horbaschek, R. Schulz, and M. Spahn, "Amorphous silicon X-ray image sensor," in *Medical Imaging 1996: Physics of Medical Imaging, Proc. SPIE* **2708**, 499–510 (1996).
46. T. Graeve, Y. Li, A. Fabans, and W. Huang, "High-resolution amorphous silicon image sensor," in *Medical Imaging 1996: Physics of Medical Imaging, Proc. SPIE* **2708**, 494–498 (1996).
47. D. L. Lee, L. K. Cheung, E. F. Palecki, and L. S. Jeromin, "A discussion on resolution and dynamic range of *a*-Se-TFT direct digital radiographic detector," in *Medical Imaging 1996: Physics of Medical Imaging, Proc. SPIE* **2708**, 511–522 (1996).
48. W. Zhao, I. Blevis, S. Germann, and J. A. Rowlands, "A flat-panel detector for digital radiology using active matrix readout of amorphous selenium," in *Medical Imaging 1996: Physics of Medical Imaging, Proc. SPIE* **2708**, 523–531 (1996).
49. J. S. Lim, *Two-Dimensional Signal and Image Processing*, Prentice-Hall, Englewood Cliffs, NJ (1990).

Til Aach received the diploma and Doctoral degree in electrical engineering from Aachen University of Technology (RWTH) in 1987 and 1993, respectively. From 1987 to 1993, he was with the Institute for Communications Engineering, Aachen University of Technology, where he was responsible for a number of research projects in medical image processing, analysis and compression of stereoscopic images, and image sequence analysis. From 1993 to 1998, he was a project leader with Philips Research Laboratories, Aachen, where he was responsible for projects in medical image processing. In 1996, he was also a lecturer with Otto-von-Guericke University, Magdeburg. As of February 1998, he was appointed a full professor of computer science and head of the Institute for Signal Processing and Process Control, Medical University of Luebeck, Germany. He is also a consultant to industry.

Ulrich Schiebel received his PhD in physics from Justus-Liebig-University, Giessen, Germany in 1975. Since 1978 he is with Philips Research Laboratories, Aachen, Germany. For more than 15 years he has been working in the field of electronic x-ray detectors for digital radiography, delivering major research contributions to the selenium-based Philips Thoravision system and *a*-Si:H flat-panel x-ray imagers. Currently he is a department head in Philips Research, responsible for the fields of luminescent materials and electron emitters.

Gerhard Spekowius studied physics at the University of Hannover (Germany) and received a PhD in 1991. His major fields of working have been multiple molecular ionization processes, photionization, laser spectroscopy, and charged particle detectors. In 1992 he joined the Philips Research Laboratories in Aachen. Since then he has been working as project leader for digital x-ray imaging with XRII/CCD camera chains and x-ray image quality modeling. His current focus is on medical displays and soft-copy image presentation.